Chemical Physics Reviews REVIEW scitation.org/journal/cpr

Strain Engineering in Metal Halide Perovskite Materials and Devices: Influence on Stability and Optoelectronic Properties

Mengru Wang, Zhenyi Ni, Xun Xiao, Ying Zhou, and Jinsong Huang*

Department of Applied Physical Sciences, University of North Carolina, Chapel Hill, NC 27599, USA.

Abstract: Metal halide perovskites (MHPs) have been extensively studied for their promising applications in solar cells and other devices due to their extraordinary optoelectronic properties, low cost, and easy fabrication by versatile processes. Different from bulk crystals grown from solutions, polycrystalline perovskite films deposited on substrates generally are strained due to multiple mechanisms, which significantly impacts their optoelectronic properties, defect physics and photostability. The fabrication and operation of perovskite solar panels inevitably introduce stains in perovskite. Strain has been broadly applied to stabilize the photoactive phase of several perovskite compositions which would otherwise show a thermodynamically stable photoinactive phase at room temperature. There is increasing research on strain engineering of MHPs to enhance device performance. However, a systematic review and understanding of strain engineering in MHP is still lacking. Herein, an overview of strain engineering on MHP materials and solar cells is provided. In this review, we start with a general review on strain in semiconductors, including the characteristics of strain, characterization techniques, and the effects of strain on the lattice structure, electronic and optical properties of semiconductors. We then summarize the progress in understanding the generation of strain categorized by local and global strains, and their impacts on the multi-facet properties of MHPs, including phase stability, photostability, and other optoelectronic properties. Both positive and negative impacts have been observed on these properties. Strain engineering has shown to be promising in making much more efficient and stable perovskite solar cells.

Key words: perovskite, strain, band structure, defect density, phase stability, efficiency

Table of Contents

I. Introduction

MHPs have attracted much attention due to their high defect tolerance, low trap density, high optical absorption coefficients, high carrier mobility, long carrier lifetime and tunable bandgap[1-6]. The low-cost, low-temperature scalable solution fabrication processes have also promoted the wide applications of MHPs in photovoltaics, light-emitting diodes, photodetectors, lasers, and ion radiation detectors[7-12]. It's notable that the power conversion efficiency (PCE) of single-junction perovskite solar cells has been rapidly enhanced from 3.8% to 25.5% in ten years[13, 14], which is higher than those of other thin film photovoltaics such as CdTe and CIGS, and is approaching the best efficiency of monocrystalline single crystal silicon solar cells.

Strain as one very important variable which defines the material's deformation plays an important role in the fundamental properties and application of semiconductors which should impact MHPs. The effect of strain on semiconductor properties has been widely exploited since the influence of strain on the intrinsic mobility of Si was first investigated in the early 1950s[15-18]. It developed into a field of strain engineering, which refers to the method of improving one or more properties of materials through mechanical deformations. Strain is a tensor to describe and quantify the deformation of a material. Generally, there are components along the diagonal (normal strain) and off-diagonal terms (shear strain) in a strain tensor. Strain in materials can also be classified into four types according to the loading applied to the material (**Figure 1a**): uniaxial strain (a material is stretched or compressed along one direction), biaxial strain (a material is pulled or compressed in two directions), hydrostatic strain (the deformation of a material in all normal directions under loading is equal and no shear components and thereby only changes the volume of the material, but not in shape), and shear strain (the deformation of a material results from forces acting along the material's two parallel surfaces.); meanwhile, due to Poisson's effect, strain was also induced in non-loading direction. A deformed material can have a combination of these different types of strain. Based on the distribution range and state of the strain, it can also be classified as global and local strains. A global strain means that the strain is introduced across the entire materials, which mainly origins from lattice mismatch or thermal

* Correspondence to J.H. (email: jhuang@unc.edu)

expansion coefficients mismatch between materials and the substrates (**Figure 1b-c**). In epitaxy growth of materials, if the lattice constant (α_1) of material 1 is larger/smaller than that of material 2 (α_2), an in-plane biaxial compressive/tensile strain is induced in material 1. For materials involving in thermal annealing processes, if the thermal expansion coefficient of materials 1 (α_1) is larger/smaller than that of material 2 (α_2), an in-plane biaxial tensile/compressive strain is induced in material 1. The deformation of substrates will also induce strain in pre-deposited materials. For example, bending the substrates could induce in-plane uniaxial tensile/compressive strain related to bending direction in materials (**Figure 1d**). Elongating the substrate could also induce in-plane uniaxial tensile strain in pre-deposited materials (**Figure 1e**). Although the range of global strain is the entire material, the global strain can be either homogeneous or inhomogeneous across the whole material. For example, thermal gradient induces inhomogeneous global strain in materials. In the epitaxial growth of semiconductors, the largest strain is at the heteroepitaxial interface and strain decreases at the regions away from the interface. As the strain energy increases, it would become energetically favorable to form dislocations. Strain relaxation occurs along with the generation of these dislocations. While bending materials to induce uniaxial strain, all materials on one side of the neutral axis are under tension, while those on the other side are under compression and there is no strain along the neutral axis. The location of neutral axis of the layered structure depends on the sample structure, including the thicknesses and mechanical properties of functional layers and substrates[19]. The bending strain is a function of bending curvature and the distance from the neutral axis: $\varepsilon=h/\rho$, ρ is the bending curvature of the material and h is the distance from the neutral axis. So, there is a strain gradient from top to bottom across the cross section and the maximum strains occurs on the material surfaces. A local strain means that the strain is not uniform through the material, only locating in certain regions. As shown in **Figure 1f**, depositing materials on elastically pre-deformed substrates firstly and then releasing the substrates result in a local strain in the wrinkling or bucking regions of the material. Besides, local strain can also be induced by elemental doping or alloying due to the size difference between the dopant and the host atoms (**Figure 1g**).

Strain in semiconductors is embodied in the extension or shortening of chemical bond lengths, and/or the change of chemical bond angles, which leads to changes in crystal volume and/or the distortion of the lattice of crystals. Such a distortion can cause a phase transition. Theoretical and experimental work have demonstrated that strain could change the crystal structure of Si, Ge and two-dimensional transition metal chalcogenides, resulting in a phase transition[20-23]. For example, a small (0.2%)

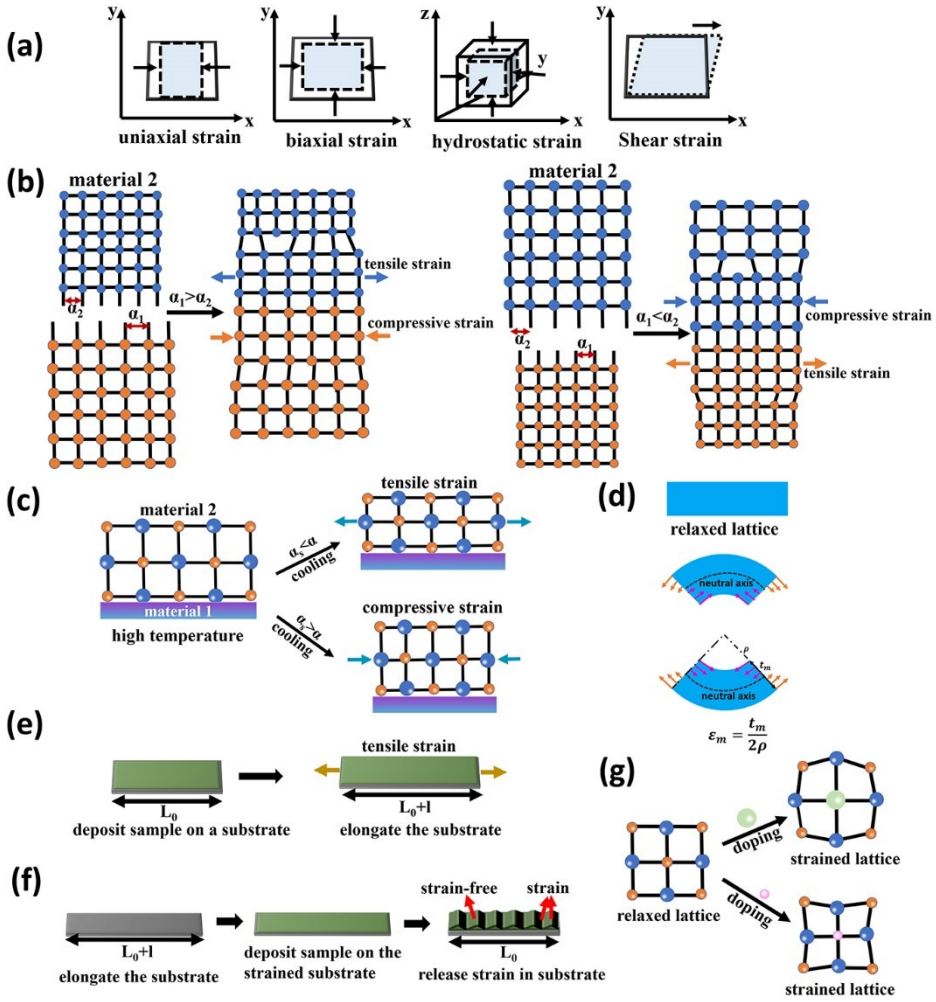

Figure 1. (a). Schematic of <100> uniaxial, (x-y) plane biaxial, and hydrostatic strain. Schematic of methods to induce strain: (b), lattice mismatch; (c), thermal expansion coefficients mismatch; (d), bending the substrates; (e), elongating substrate to induce uniaxial tensile strain; f), releasing strain in the pre-deformed substrate. (g), chemical doping or substitution or absorption.

tensile strain has been shown to transform hexagonal semiconducting $MoTe_2$ (~1 eV bandgap) into metallic phase (distorted octahedra)[23]. The changed lattice constant by strain should change the interatomic interaction as well, resulting in a change in bandgap. For example, in most semiconductors, a compressive strain would make the bonding and antibonding energy states further apart in energy, resulting in a wider bandgap. Furthermore, the influence of strain on the conduction band and valance band may be different, and thus induces direct-indirect transitions in semiconductors such as two dimensional MoS_2[24-26]. At the same time, the changed band structure in strained semiconductors inevitably impacts the curvature of the dispersion relation at the band edges. The effective mass (m*) of carriers is determined by the band curvature, and thus changes with strain which also impacts carrier mobilities. For example, the carrier mobility in Si NWs is very responsive to strain and can be enhanced or reduced by a factor 2-5 for moderate uniaxial strains within the ±2% range due to the changes in the effective mass (m*) of carriers[24]. Strain can also impact the defect density in materials. Strain could change the vacancies concentration in semiconductors by changing its formation energy. For example, the tensile strained MoS_2 has a decreased bandgap and increased S vacancy concentrations[27], leading to an unprecedentedly catalytic activity of MoS_2 for the hydrogen evolution reaction. Strain has also been proved to control the O vacancy concentrations by changing the formation energy of O vacancies in transition-metal oxide materials[28, 29]. For example, the oxygen content of perovskite-based strontium cobaltite ($SrCoO_{3-x}$) shifts from $x<0.1$ to $x\sim0.25$ when modest amounts of tensile strain over 1% was induced in materials[28].

Strain engineering is an effective tool to tune material properties for its pronounced impact on lattices. Notably, strain in semiconductors is inevitable introduced in material fabrication for either lattice mismatch with substrates or lattice expansion/contraction during thermal annealing process. Hence, studying the strain effect would provide insights in understanding and designing MHPs for solar cell applications. Compared with traditional semiconductors such as Si and GaAs, MHPs have a relatively low Young's modulus (10-30 GPa) and a large ratio of bulk modulus to shear modulus (bulk modulus/shear modulus >1.75), which may enable flexible perovskite devices, including flexible solar cells, light emitting diode and detectors[30-33]. The soft nature of MHPs makes them more sensitive to stress than other semiconductor materials, since the strain is greater under the same stress in MHPs. Residual tensile strain has been commonly observed in thermally annealed perovskite films[34, 35]. Changing local strain using alloying has been shown to successfully enhance the performance of perovskite solar cells, including efficiency and stability[36]. Therefore, strain engineering in perovskite has aroused great interest of research. This review summarizes the progress in understanding the effect of strain on phase stability, band gap and trap density in MHPs, and future research prospectus.

II. Strain Characterization

The first step to understand the impact of strain on materials is to accurately characterize the strain. The strain in semiconductors can be directly characterized through the lattice distortion by X-ray diffraction (XRD) and transmission electron microscopy (TEM) measurements. And it can also be indirectly quantified through the changes of the optical properties of semiconductors that characterized by Raman spectroscopy. Here, we summarize these three commonly used techniques for strain characterizations.

X-ray diffraction: XRD technique is a widely used method to characterize lattice structures with high resolutions, which can directly measure the global strain without the destruction of the sample[37]. Strain in materials will induce lattice contraction/expansion or tilting. Correspondingly, XRD peaks shift to a larger/smaller diffraction angle under compressive/tensile strain. In addition, the diffraction peak is broadened when the strain is not homogeneous in materials. Moreover, X-ray microdiffraction method was employed to measure the strain with a sub-micro spatial resolution, which is three orders of magnitudes higher than that of conventional XRD techniques, and the strain-resolution ($\Delta\varepsilon$) reaches 10^{-5}.[37, 38] Generally, X-ray technique requires a volume of materials (more than tenths of a gram), therefore it is unfeasible for the analysis of the lattice information of individual nanosized materials.

TEM: TEM technique is a powerful technique to characterize strain which typically has a spatial resolution up to 0.1-0.2 nm with a precision 10^{-3}.[39] Strain is characterized by measuring the changes in local lattice constants and orientations of the lattice planes with respect to reference materials. Considering the immediate damage of the materials by the energetic electron beam, cryo-TEM has been applied in the structural characterization of materials that are prone to be damaged by electron beam (e.g., perovskites)[40, 41]. In addition, low-dose scanning TEM is also used to determine the microstructure of perovskite thin films to slow down the degradation from the same total electron beam[42]. Notably, it is still challenging to prepare TEM samples, which should be thin enough to become sufficiently transparent to electrons. The samples are usually thinned by ion-beams, which may introduce damages or changes to the strain of samples, leading to an inaccurate characterization of the strain[39, 43].

Raman spectroscopy: Raman Spectroscopy is a non-destructive chemical analysis technique to study the stress/strain of materials based on the interaction of the laser with the chemical bonds in a material[44]. Strain in materials leads to the changes in lattice vibration (phonon) which can be detected out by Raman Spectroscopy. The vibrational frequency shift is shown to be proportional to strain magnitude in materials[45-49]. In tensile strained materials, phonon softens and the vibrational frequency decreases in the strain direction, leading to a red-shifting of the Raman peaks. Conversely, compressive strain leads to phonon hardening and a blue-shifting of Raman peaks[45]. The capability of mapping using Raman allows the mapping of strain with a spatial resolution better than 0.5 μm and a sensitivity better than 10^{-3}.[44] Also, it does not require sophisticated sample preparation, ensuring undistorted strain states in materials. In Raman spectroscopy, great considerations should be paid to the excitation laser wavelength and intensity, because they affect both the Raman signal depth profile and intensity[50]. In addition, low-power laser is needed to avoid laser-heating effects and sample degradation. For example, the laser excitation power with less than 10 μW on spot diameter of 1 μm was reported in Raman measurement of laser-sensitive perovskites, which is 2 orders of magnitude lower than μc-Si:H thin films[51, 52].

It should be noted that the Raman peak shifting is not only related to the strain in materials, the changes of physical or chemical environments also will cause the shifts of Raman peaks. The dependence of peak frequency and full width at half-maximum (FWHM) on defect density and grain sizes have also been demonstrated[53]. Therefore, it is important to control experimental conditions precisely and combine other strain characterization methods to characterize strain in materials.

III. Strain Engineering in Metal Halide Perovskites

A. Strain in perovskites

1. Local strain

In ABX_3 structured perovskites, the mismatch between the A cations and BX_6 cage size leads to cage distortions and BX_6 octahedra tilting, inducing local strain in perovskites. In perovskites, Goldschmidt's tolerance factor (τ) is widely used in predicting the structural stability and Octahedral factor (μ) defines the stability of the BX_6 octahedron[54]. Both factors are necessary but not sufficient to predict perovskite structural formability. Tolerance factor τ can be expressed by the equation: $\tau=\frac{R_A+R_X}{\sqrt{2}(R_B+R_X)}$; where R_A, R_B and R_X are the ionic radii of A cation (methylammonium-MA^+, formamidinium-FA^+, Cesium-Cs^+, etc.), B cation (lead-Pb^{2+}, tin-Sn^{2+}, etc.) and X anion (iodide-I^-, bromide-Br^-, chloride-Cl^-, etc.), respectively. Octahedral factor μ is the ratio of the ionic radius of B and X atoms: $\mu = \frac{R_B}{R_X}$. Perovskites with τ between 0.8 and 1.0 and u between 0.44-0.90 are reported to be thermodynamically stable at room temperature[54, 55]. However, perovskites with τ out of this range, such as $FAPbI_3$ (τ >1) and $CsPbI_3$ (τ <0.8), tend to form the photoinactive hexagonal δ-phase at room temperature. During the spontaneous phase transformation from photoactive perovskite phases to δ- phases, strain is also induced in crystals due to the spatial heterogeneity. Saidaminov et al. claimed the existence of local strain in black-phase $FAPbI_3$ (α-$FAPbI_3$) and it would be released by point defect formations[36]. On the other side, Zheng et al. proposed that α-$FAPbI_3$ has an anisotropic strained lattice and the strain in the (111) plane is greater which drives phase transformation into the strain-free δ-phase[56]. The unfavorable residual strain in $FAPbI_3$ lattice could be released by the substitution or doping of foreign ions (such as MA^+, Cs^+, Ca^{2+}, Cl^- or Br^-) to form alloyed perovskites[36, 56-59]. However, composition inhomogeneity in alloyed perovskites also leads to local strains. For example, I-Br mixed halide perovskites tend to form I-rich regions and Br-rich regions under illumination when the content of Br is larger than 20%[60], which would induce local strain in perovskites. In polycrystalline perovskite films, grain boundaries are known as reservoirs of defects and likely to change the strain state in their vicinity because of different atomic spacing and structure compared to their perfect crystal structure[61]. In addition, light-induced strain is also reported in $FA_{0.7}MA_{0.25}Cs_{0.05}PbI_3$ and $MAPbI_3$ films[62, 63], originating from photothermal-induced expansion in the perovskite films. Solid material formation kinetics also impact the residual strain in films or crystals. For example, strain can be induced in solution-processed films due to solvent removal, phase transformation from intermediate phases, film shrinkage, and volatile component (MA^+, Cl^-) removal during annealing[64]. Therefore, strain distribution is likely to be inhomogeneous at atomic scale in perovskite materials. Jones et al. probed local strain in $MAPbI_3$ perovskite thin films by scanning micro-XRD (μXRD) and high-resolution TEM. The spatial resolution of the μXRD was ~2.5 um. Subtle shifts in the <220> and <222> diffraction peaks position and broadening illustrated the occurrence of local structural heterogeneity on the scale of beam resolution. The strain map for the <220> diffraction peak showed that the magnitude of strain is 0.1–0.2%. They also collected the high-resolution TEM images from a 70×70 nm^2 region. The electron dose rate of TEM was ~1-4 electrons $Å^{-2}$ s^{-1}. There were different diffraction patterns from various 10×10 nm^2 regions of the TEM images, demonstrating the presence of structural heterogeneity in nanoscales[65]. Local strain in perovskite films is very complicated, and thus need a much more comprehensive characterization to provide insight into how the local strain is controlled by film formation kinetics, material composition, material morphology, etc.

2. Global strain

a) Thermal effect: Thermal expansion coefficient mismatch between perovskites and substrates introduces global strain in perovskite films during their fabrication processes. The thermal expansion coefficients of perovskites are approximately one order of magnitude higher than most of their substrates and charge transport materials (e.g., ITO glass, Si, SnO_2, TiO_2, PTAA, etc.)[34, 35, 66-70]. In 2017, Zhao et al. first discovered that MHP films fabricated by all methods that involve thermal annealing, including one-step spin-coating, two-step spin-coating, and doctor blade–coating, were strained, and the flat polycrystalline $MAPbI_3$ films have an in-plane tensile strain of 0.47% after cooling down from 100 °C[34]. The clamp effect of the substrate also induces a compressive strain along the out-of-plane direction due to the Poisson effect. Rolston et al. also reported a residual in-plane tensile stresses in perovskite films in excess of 50 MPa which is high enough to deform copper[35]. Steele et al. used synchrotron-based, grazing incidence, wide-angle x-ray scattering to monitor the crystal distortion process in $CsPbI_3$ thin film after it rapidly cooling from 330 °C to 100 °C, and observed a ~1% in-plane tensile strain[71]. The magnitude of strain from thermal expansion coefficient mismatch directly correlates with the annealing temperature of perovskite films. Reducing the film stress and strain can be accomplished by decreasing annealing temperatures or selecting substrates with large thermal expansion coefficients[35, 72]. In addition, the residual tensile strain can be compensated by introducing a compressive strain. The poly [5,5-bis(2-butyloctyl) -(2,2bithiophene)-4,4′-dicarboxylate-alt-5,5′-2,2′-bithiophene] (PDCBT), possessing a higher thermal expansion coefficient than perovskites, has been used as the hole transport layer in n-i-p solar cells structure. The tensile strain in PSCs was compensated by elevating the processing temperature of hole-transport layer, leading to a non-strained or even compressively strained $CsPbI_2Br$ perovskite film[72].

b) The epitaxial growth of perovskite: In perovskite solar cells, lattice mismatch induced strain is not inevitable, because the growth of perovskite on charge transport layers or charge transport layers on perovskite is not epitaxial in most of cases[73-76]. However, there are cases epitaxial growth can occur. The horizontal growth of strained $CsPbBr_3$ microwires on sapphire substrates has already been reported, where the $CsPbBr_3$ (110) plane grows on the sapphire (0001) plane and the in-plane lattice parameter of $CsPbBr_3$ is enlarged by ~2% at the interface with sapphire[74]. Chen et al. reported the strained epitaxial growth of halide perovskite single-crystal thin films on lattice-mismatched halide perovskite substrates[73]. They investigated the strain in α-$FAPbI_3$ that was epitaxially grown on $MAPbCl_xBr_{3-x}$ single crystal substrates with different compositions. An in-plane biaxial compressive strain as high as 2.4% was detected in the epitaxial α-$FAPbI_3$. Chen et al. studied confocal photoluminescence spectra at different locations in an α-$FAPbI_3$ film of around 3 μm thick grown on a $MAPbCl_{1.5}Br_{1.5}$ single crystal substrate and founded that the 2.4 % compressive strain decreased to near zero from the interface of α-$FAPbI_3$/ $MAPbCl_{1.5}Br_{1.5}$ to the top surface of α-$FAPbI_3$. It was because that strain in the epitaxial α-$FAPbI_3$ is determined not only by the lattice mismatch between the epilayer and substrate, but also the strain relaxation mechanisms. The thickness-dependent in-plane XRD showed that the critical thickness of the 2.4% compressive strained α-$FAPbI_3$ film is much smaller than 3 μm, which is close to 100 nm.

In addition, the epitaxial growth of α-$CsPbBr_xI_{3-x}$ perovskite after adding PbS colloidal quantum dots (CQDs) in $CsPbBr_xI_{3-x}$ films has been reported[77]. The crystal structure and the orientation of perovskites relative to PbS CQDs were investigated by high-resolution TEM. They observed the formation of a perovskite shell at high PbS CQD concentration

and there was no spacing difference between the core CQD and the $CsPbBr_2I$ perovskite shell at $(1\bar{1}1)$ and (200) planes, indicating the epitaxially orientational alignment of $(1\bar{1}1)$ and (200) planes for both PbS CQDs and for the $CsPbBr_2I$ (**Figure 2a**). Lattice mismatch increases as decreasing the ration of Br in $CsPbBr_xI_{1-x}$, generating a larger strain at interfaces[77]. It was also reported that the epitaxial growth of α-$FAPbI_3$ phase was observed during its phase transformation from the hexagonal δ-$FAPbI_3$ when it forms epitaxial heterostructure with $FPEA_4PbI_4$ layered perovskite[76]. After adding $FPEA_4PbI_4$ layered perovskites in $FAPbI_3$ perovskite films, TEM images (**Figure 2b**) showed that the (002) plane of the layered perovskite was aligned with the (010) plane of the δ-$FAPbI_3$ phase and the larger interplanar spacing of the δ-$FAPbI_3$ indicates the presence of tensile strain at the interface with the layered perovskite. Meanwhile, a semi-coherent interface between the layered perovskite and the α-$FAPbI_3$ was observed, where the (111) plane of the grown α-$FAPbI_3$ orientationally aligns with the (002) plane of the layered perovskite, implying that the heteroepitaxial growth of the α-$FAPbI_3$ crystals occurs during the phase conversion process and the compressive strain was applied to the interfacial α-$FAPbI_3$ phase[76].

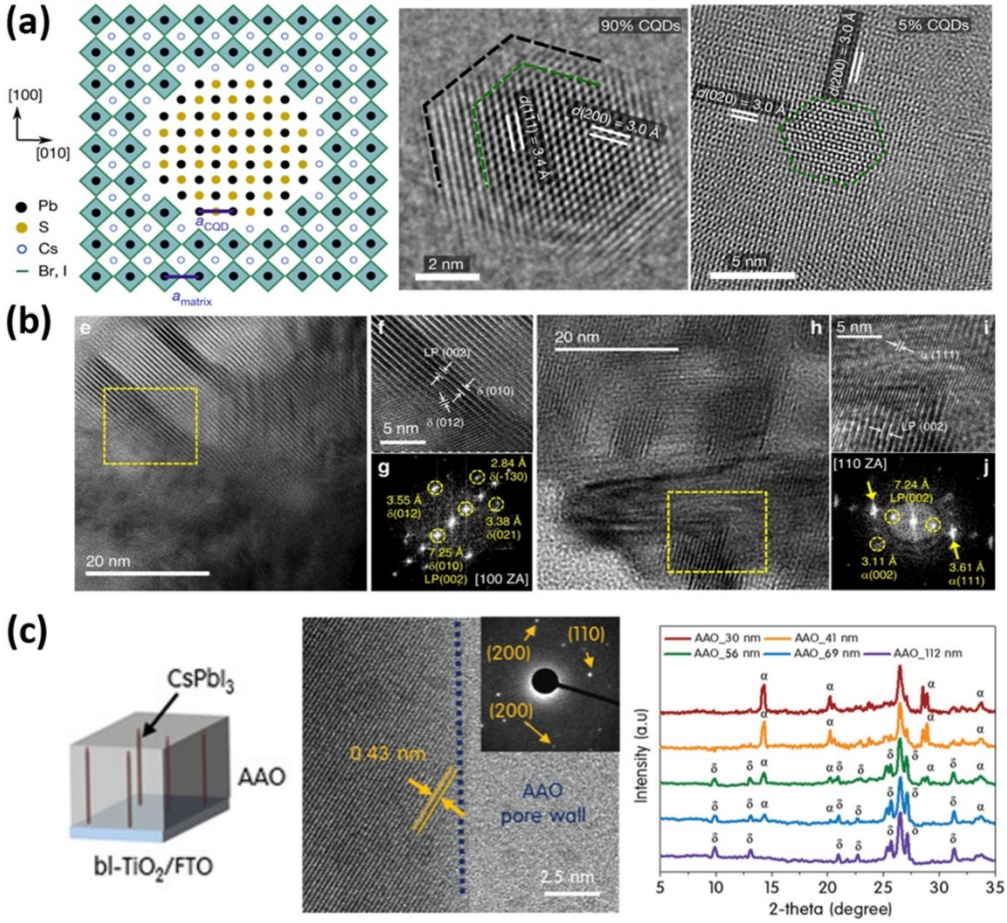

Figure 2. (a), Schematic depiction of the atomistic model of a PbS CQD:perovskite lattice-anchored hybrid materials system and High-resolution TEM images of the lattice-anchored PbS CQD:perovskite hybrid materials at high (up) and low (down) CQD concentration[77]; Reproduced with permission from Nature 570, 96-101 (2019). Copyright 2019 Nature Publishing Group. (b), High-resolution TEM images and corresponding fast Fourier transform analysis of $FAPbI_3$ films incorporated with $FPEA_4PbI_4$ before (left) and after the phase conversion process (right)[76]; Reproduced with permission from Nat Commun. 11,1 (2020). Copyright 2020 Nature Publishing Group. (c), High-resolution TEM image of $CsPbI_3$ perovskite confined in an AAO template with a pore size of 41 nm (left) and XRD patterns CsPbI3 perovskite thin films confined in AAO templates (right)[80]. Reproduced with permission from Small 15, (2019). Copyright 2019 Wiley-VCH.

c) Interface (not epitaxy) /surface stress: Zhao et al. fabricated large-grained $CsPbBr_3$ perovskite films by two-step sequential deposition fabrication method and observed the compressive stress along the in-plane direction. The compressive stress is higher enough to induce strain in $CsPbBr_3$ perovskite films. The compressive stress originated from lattice mismatch between $PbBr_2$ to $CsPbBr_3$ due to the lattice volume is enlarged by 2.18 times during the phase conversion from $PbBr_2$ to $CsPbBr_3$ perovskite[78]. In addition, lattice mismatch between perovskite lattices and large cations introduced on the surface of perovskites, like PEA^+, GA^+, also induces strain to perovskite films. The soft cation framework of large organic cations buffers the lattice deformation under residual stress in perovskite films[79].

Ma et al. noted that strain was imposed to α-$CsPbI_3$ perovskites when they were confined in vertically aligned nanopores of anodized aluminum oxide (AAO)[80]. As shown in **Figure 2c**, high-resolution TEM showed that perovskite crystals were confined within 41 nm-size pores of AAO template, and the (110) plane was sloped at an angle of 35.5° with respect to the AAO pore wall. XRD results exhibited a reduce in the peak intensity (200)/(110) ratio, indicating enhanced growth of the (110) plane while suppressing the growth of the (200) plane.

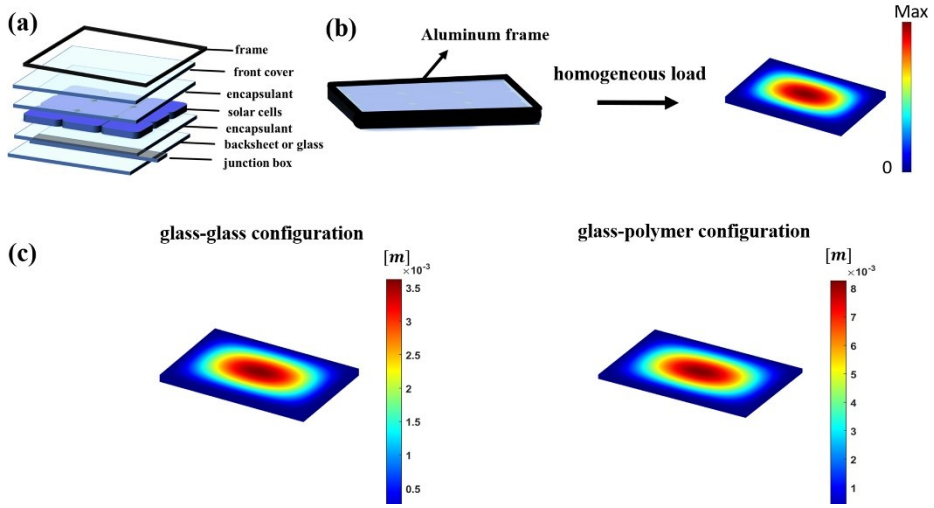

Figure 3. (a), Structure of PV modules. (b), Displacement distribution on solar panels framed by perimeter under a homogenously distributed load on the front cover. (c), Displacement distribution on glass-glass and glass-polymer solar panels framed by perimeter under 1000 Pa on the front cover.

They thought that the compressive stress imposed by the pore walls was imposed on the [010] and [001] directions of the perovskite lattice, suppressing the growth of the (200) plane parallel to the pore wall. The compressive stress made the dominant growth orientation of α-$CsPbI_3$ change to the stress-free [100] direction. The strain magnitude is dependent on the nanopore size of the AAO template. External mechanical stress induced strain, by hydrostatic pressure and bending substrates, has also been reported[81-85].

In perovskite nanoparticles, strain mainly come from its high surface tension due to the large surface-to-volume ratio. The tension and strain magnitude depend on the size of perovskite nanoparticles[86]. One the other hand, Zhao et al. used synchrotron radiation X-ray diffraction to analyze different shaped $CsPbBr_3$ nanocrystals with the same fabrication processes and observed the increasing trend in strain values of the nanocrystals: nanocube, nanoplate, nanowire. They thought that the strain reflected the mechanical response of $CsPbBr_3$ nanoparticles to the stimulus from surrounding liquid organic ligands and the result was in good agreement with the nature that nanowires are easier than nanocubes for bending[87]. Size-dependent and/or shape-dependent strain in perovskite nanoparticles and its effect on nanoparticle properties and devices are interesting topics and need to be further understood in the future.

d) Ferroelasiticity and the photostrictive effect: Some MHPs have been determined to be ferroelastic which can change strain in perovskites with an intrinsic path. When an external stress is applied, the ferroelastic perovskite would dissipate the strain energy by forming twin structures[88, 89]. This effect makes the strain imposed by external stress to be difficult to be determined, and should be paid attention to in research. In addition, the photostrictive effect of halide perovskites has also been reported, and the photostrictive response was proportional to the light intensity[90, 91]. However, the photostrictive effect of perovskites has been raised to be an experimental artifact which can be caused by the thermal expansion from the photothermal effect was underestimated. To distinguish the contribution of strain from photostriction and thermal expansion under light in halide perovskites, Chen et al. turned the light (100 $mW.cm^{-2}$ white LED) on and off when the device temperature was kept constant[63]. It has been found that switching the light between on and off conditions for 10 minutes has no influence on the position of XRD peaks of $MAPbI_3$ when temperature was kept constant. In addition, comparing the thermal expansion and photostriction on a millisecond timescale, it was still found the thermal expansion dominated the light induced strain in $MAPbI_3$, with no photostriction detected within equipment sensitivity limitation[92].

e) Device encapsulation and operation: Photovoltaic (PV) modules need to be encapsulated. In the encapsulation process, a high temperature of > 100 ºC is generally required to cure the encapsulant, and then assembled layers are pressed together in a laminator to remove air. During this process, global strain may be introduced into perovskite and other layers due to the difference in thermal expansion coefficients of different layers. In addition, pressure from the laminator can also cause the deformation of the materials.

In operation, the working temperature of solar cells varies with environmental conditions. The environmental temperature can vary from -40 °C in arctic areas to 85 °C in desert areas. In addition, the average temperature in desert areas can be up to 40 °C during the daytime and falls to -4 °C during nighttime[93-96]. The capability of solar cells to keep their integrity is generally examined in temperature cycling test part of stability evaluation, however their impact to the strain in perovskites and other function layers have not been studied yet. Besides, hail, snow, and wind in the environment and other external mechanical loads can also deform the large solar panels. PV modules are mounted onto a support framework, resulting in the constrains of displacement and rotation of them. As shown in **Figure 3b**, a PV module is fixed on a metal framework by framing perimeters where a homogeneous distributed load is applied on the front cover of PV modules to simulate snow or wind. Using finite element simulation by MATLAB, we show that maximum strain occurs in center of the PV modules and there is no strain at the constrained region.

Different supporting systems (rigid and flexible) should also have varied effect on strain in PV modules. For flexible frames, strain also occurs in the attached areas in PV modules due to higher flexibility and lower constraint on deformation[97]. As shown in **Figure 3c**, strain in glass-polymer PV modules is larger than that of glass-glass PV modules when applying same homogeneously distributed load (1000 Pa). What is more, strain in PV modules could come from the weight of the module itself. When only weight of the module is considered, strain in glass-glass PV modules is larger than that of glass-polymer PV modules. More simulation can be found elsewhere on thermal and mechanical stress-strain in Si PV modules[98, 99]. The research on strain in perovskite solar cells still at its early stage which

focused on strain engineering in perovskite films. More research at later stage is needed to find out the strain generation and distribution in perovskite PV modules and its impact.

Table 1 lists the strain, its magnitude and influence in metal halide perovskites from recently published experimental work.

Table 1. Strain and its magnitude in metal halide perovskites from published experimental work.

perovskite	strain origin	strain magnitude and state (tensile strain +, compressive strain -)		strain type	strain effect	ref.
$MAPbI_3$ film	thermal expansion/ bending	0.2%~0.62%	in-plane tensile strain	global	Thermal expansion induced in-plane tensile strain in perovskite films; Tensile strain decreased the activation energy of halide migration and accelerated the degradation of perovskites.	34
$MAPbI_3$ film	thermal expansion	-0.30%	out-of-plane compressive strain	global	Strain patterns have a complex heterogeneity across multiple length scales, strain has a complex local heterogeneity with a magnitude of 0.1–0.2%; Lattice out-of-plane compressive strain is directly associated with enhanced defect concentrations and non-radiative recombination.	65
$CsPbBr_3$ film	thermal expansion	-1.02%	out-of-plane compressive	global	Out-of-plane strain measured via nano-XRD varies between −0.8 and −1.6%; Nanoscale residual strains negatively affect the stability of perovskites.	66
$CaPbI_3$ film	thermal expansion	1%	in-plane tensile strain	global	Cooled $CsPbI_3$ film from 300° to 100°C introduced an in-plane biaxial tensile strain of ~1%; Strain stabilized black perovskite phase due to different energy penalties for two phases: Black phase transformed to the yellow phase through strain release.	71
$CsPbI_2Br$ film	thermal expansion	-1.5%~1%	in-plane strain	global	The activation energy of halide ion migration increased, and phase separation was suppressed under compressive strain; PCE enhanced from 14.8% (tensile strain), 15.5% (strain-free) to 16% (compressive strain); Compressive-strain and non-strain devices retained 96 and 80% of their initial PCEs after 1000 h of heating at 85 °C.	72
$Cs_{0.05}MA_{0.16}FA_{0.79Pb}(I_{0.83}Br_{0.17})_3$ film	thermal expansion		in-plane tensile	global	Thermal expansion induced in-plane tensile strain and accelerated the degradation of perovskite films; High film stress increased mechanical fragility of perovskite.	35
$FAPbI_3$ film	lattice mismatch	-2.4%~0	in-plane strain	global	Compressive strain stabilized black FAPbI3 phase over 360 days at room temperature: Strain modulated bandgap of $FAPbI_3$; Compressive strain enhanced the carrier mobility prominently.	73
$CsPbBr_3$ nanowire	lattice mismatch		out-of-plane compressive	global	Lattice distortion originated from heteroepitaxial mismatch, accentuated by thermal expansion coefficients differences; Strain modulated bandgap and caused PL peak shift of nanowire.	74

$FAPbI_3$ film/ $FPEA_4PbI_4$	Lattice mismatch			local	The layered perovskite-templated epitaxial crystal growth was induced during the phase transformation of δ-α-phase; Tensile strain is existed at the interface between δ- and layered perovskite; after phase transition process, compressive strain was induced in the interfacial α phase. Strain increased the phase transition energy barrier, retarding the phase conversion kinetics.	76
$CaPbI_3$ film	AAO pore wall -stress	-2.5%~0	in-plane strain	global	Compressive strain decreased surface formation energy of the α-phase; Compressive strain stabilized α-phase over three months under ambient conditions; Compressive strain extended the carrier lifetime.	80
$CsPbBr_3$ film	lattice mismatch		compressive stress	global	Precise stress control of $CsPbBr_3$ film by controlling the crystallization temperature of $PbBr_2$ film; Reduced defect-induced charge recombination and enhanced charge transfer under suitable stress.	78
$FAPbI_3$ film	ion size mismatch			local	Strain relaxation in $FAPbI_3$ by forming point defect; Introducing smaller ions, MA/Cs or Br/Cl stabilized perovskite phase and enhanced film stability.	36
$(FAPbI_3)_{0.85}(MAPbBr_3)_{0.15}$ film	A site incorporation		in-plane strain	global	A site alloying at the surface lattice of perovskite film leads to relaxation of interfacial residual stress; Stress relaxation reduced traps on the surface and enhance stability of perovskite films.	58
PbS CQD: $CsPb(IBr)_3$ film	Lattice mismatch			local	The lattice match between QDs and α-phase suppressed the transition to the undesired δ-phase; Perovskite films remained stable for more than six months at ambient conditions; Carrier mobility was twofold due to a reduced energy barrier for carrier hopping.	77
$(CH_3(CH_2)_3NH_3)_2(CH_3{-}NH_3)_{n-1}PbnI_{3n+1}$ film	bending	0-1.18%	uniaxial tensile strain	global	Tensile strain increases the optical band gap at a rate of 13.3 meV/%.	85
$(PEA)_2PbI_4$ singe crystal	hydrostatic pressure		compressive strain	global	Ultrabroad tunability of ~320 meV by a moderate pressure ranging from 0 to 3.5 GPa.	100
$MAPbBr_3$ single crystal	thermal expansion	-0.3%-0.3%	in-plane strain	global	Crystal lattice can strain, relax, or compress as the annealing temperature varies; HOMO levels changed under different strain; The carrier mobility, photocurrent, charge carrier lifetime enhanced under 60± 55 ℃.	101

B. Impact of strain on properties of perovskites

1. Influence of strain on perovskite structures

a) Phase transition: Strain engineering of perovskites could induce the deformation of the crystal structure or phase transitions by distorting the inorganic frameworks. In the strained epitaxial growth of α-$FAPbI_3$ films on lattice-mismatched single crystal perovskite substrates, reciprocal space mapping of strain-free and strained α-$FAPbI_3$ thin films showed that the increase of the tetragonality of the lattice is evident as the compressive strain increases[73]. Under hydrostatic pressures, most of perovskite single crystals, like $MAPbI_3$, $MASnI_3$, $FAPbI_3$, $CsPbI_3$, $CsPbCl_3$, $(PEA)_2PbBr_4$, have been reported to undergo phase transition processes, then become amorphous under higher

pressures (e.g., 4.1 GPa for $FAPbBr_3$ single crystal)[102, 103]. The magnitude of the pressure needed to induce phase transition and amorphization is different for halide perovskites with different compositions and lattice symmetries which have different bulk moduli and elastic moduli.

b) Thermodynamics and kinetics of perovskite stability:

(1) thermodynamics of phase stability: Modulating strain is a promising strategy to stabilize photoactive perovskite phases. In perovskites with tolerance factors out of the range 0.8 ~ 1, local strain can be changed by incorporating foreign ions, successfully establishing an energetically stable photoactive alloyed perovskite[36]. In addition, it has also been observed that the freshly fabricated black photoactive pure phase perovskite films can be stable on substrates at room temperature for a few minutes. However, once they were scraped from the substrate, they would turn into yellow phase immediately[34, 71]. Compared to the strain-free perovskite powders, perovskite films on the substrate have a biaxial tensile strain due to the thermal expansion coefficient differences between the perovskite and the substrate. In $CsPbI_3$ perovskite, the introduction of ~1% in-plane biaxial strain leads to different free energy changes for the orthorhombic γ-phase (ΔE=4 meV) and hexagonal δ-phase (ΔE=31 meV), making the energy difference promoting the γ-to-δ transition decrease from 85 meV to 58 meV, thus improving the phase stability of γ-phase $CsPbI_3$ **(Figure 4a)**[71]. Meanwhile, the compressive strained epitaxial α-$FAPbI_3$ thin film exhibits long-lasting phase stability at room temperature[73]. As shown in **Figure 4b**, the sub-100 nm epitaxial α-$FAPbI_3$ thin film with in-plane 2.4% compressive strain is stable for at least 360 days at room temperature. In contrast, the strain-free α phase $FAPbI_3$ immediately turns into the yellow δ phase in only one day. Chen et al. proposed two possible mechanisms for the stability of epitaxial α-$FAPbI_3$ films: the interfacial energy of the α-$FAPbI_3$/$MAPbCl_xBr_{3-x}$ single crystal substrate is lower than that of the δ-$FAPbI_3$/$MAPbCl_xBr_{3-x}$ single crystal substrate; The compressive strain in the epitaxial α-$FAPbI_3$ neutralizes the effect of an internal tensile strain, which would induce the formation of vacancies and subsequent phase transition.

(2) phase transition energy barrier: The influence of strain on the energy barriers for the phase transition between the α-$FAPbI_3$ and δ-$FAPbI_3$ was calculated based on the density functional theory (DFT). The calculations confirmed the existence of a potential barrier for the phase transition between α-$FAPbI_3$ and δ-$FAPbI_3$[103]. Lee et al. found that strain increases the phase transformation energy barrier height of α phase to δ phase and when the $FAPbI_3$ interlayer spacing decreases from 15.48 Å toward the 15.26 Å, the energy barrier height increased by ~0.15 eV from the DFT calculations (**Figure 4c**)[76]. The increase of energy barrier between α-δ phase will be beneficial for the thermodynamic stability of the α-phase at room temperature. In conclusion, strain engineering can stabilize photoactive perovskite phase.

(3) Ion migration: In strained halide perovskites, local tensile strain reduces the stability of the photoactive perovskite through strain relaxation by the formation of

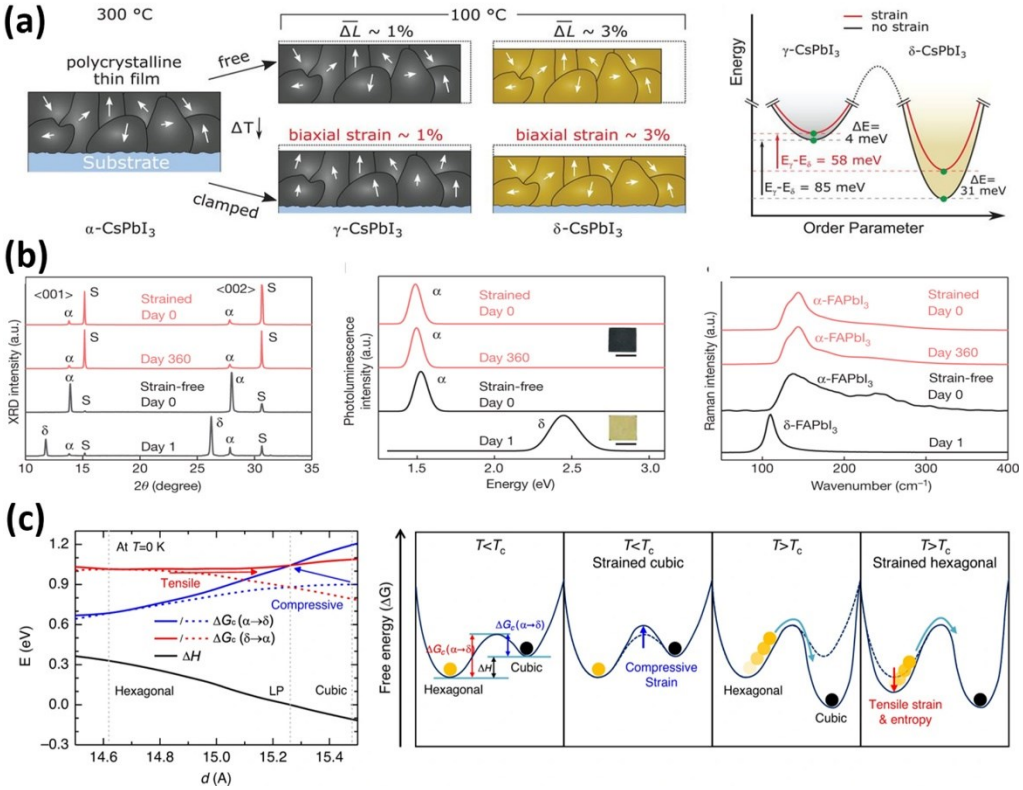

Figure 4. (a), Ab initio energy diagram of the black and yellow $CsPbI_3$ phases with and without in-plane biaxial strain[71]. Reproduced with permission from Science **365** (6454), 679-684 (2019), Copyright 2019 American Association for the Advancement of Science. (b), Phase stability comparison of strained $FAPbI_3$ film and unstrained $FAPbI_3$ film[73]. Reproduced with permission from Nature 577, 209-215 (2020), Copyright 2020 Nature Publishing Group. (c), DFT-calculated free energy barriers (ΔGcs) for phase conversion (left) and schematic free energy diagrams for the δ- and α- phased $FAPbI_3$ at compressive strain condition (right) and schematic free energy diagrams for the hexagonal and cubic phased $FAPbI_3$ at different temperatures and strain condition[76]. Reproduced with permission from Nat Commun. 11,1 (2020). Copyright 2020 Nature Publishing Group.

point defects[36]. These point defects may be the energetic active sites to react with water and oxygen molecules, thereby accelerating the degradation of perovskites. In addition, tensile strain will reduce the stability of perovskite by accelerating the ion migration, even though it can stabilize α-$FAPbI_3$ perovskite phase by suppressing the phase conversion to δ- phase. Zhao et al directly measured the ion migration activation energy by temperature conductivity of perovskites under different strain status, and verified that the tensile strain in MHPs reduces the activation energy of ion migration[34]. **Figure 5a** shows schematic diagram of the different strained $MAPbI_3$ films by bending substrates. The in-plane biaxial tensile strain in the flat film is about 0.47%. The films were bent in a convex shape to increase the strain to 0.62% or in a concave shape to reduce the strain to 0.2%. When exposing the encapsulated strained film to ~50 mW/cm^2 illumination at 65 °C, the films with 0.63% tensile strain had large areas turned yellow with the appearance of strong PbI_2 peaks, whereas the films with the almost zero tensile strain remained mostly black without any appearance of the PbI_2 peak after 500 hours illumination. The accelerated degradation by strain is related to the change of ion migration under strain. In the dark, the activation energies for ion migration are 0.29, 0.39, and 0.53 eV, respectively, and 0.046, 0.074, and 0.083 eV, respectively, under 25 mW/cm^2 white illumination when tensile stain are 0.62%, 0.47% and 0.2%, respectively. The result conclusively shows that the perovskite films with larger tensile strain have smaller ion migration activation energy in both dark and under illumination conditions. The ion migration accelerates the decomposition of perovskites.

The ion migration will lead to the phase segregation in mix-halide perovskites, which is detrimental to perovskite material stability. Liu et al. obtained near strain-free colloidal PbS quantum dots (CQDs)-$CsPbBr_2I$ perovskite interface. They observed that phase segregation occurred in pristine $CsPbBr_2I$ perovskite films within 30 min after annealing in air at 200 °C. However, this was largely suppressed when PbS CQDs are integrated in $CsPbBr_2I$ at a concentration above 6%, and no film degradation was observed after 5 hours[77]. The intensity loss in absorbance and the shift in the absorption edge of unencapsulated CQDs-$CsPbBr_xI_{1-x}$ after 5 hours of annealing in air (x is the Br content) are shown in **Figure 5b**. For PbS CQD: $CsPbBr_2I$ (x~66%) samples in which near zero lattice mismatch is achieved at the interface of PbS CQDs-$CsPbBr_2I$, film stability shows a gradual improvement with increasing CQD concentrations. Ehrler et al. found that when the hydrostatic pressure applied to the perovskite film was increased to 0.3 GPa[81], the formation rate of iodide-rich and bromide-rich phases in $MAPb(Br_xI_{1-x})_3$ decreased by two orders of magnitude. The results are consistent with calculational work about the tendency of activation energy for ion migration with strain. The migration barrier of ions increases under compressive strain and decreases under tensile strain[105]. Compressive strain shortens the length of the Pb-I bond and enhances the interaction between Pb and I atoms, making it difficult for I ions to escape from the lattice. As the activation energy for ion migration increases, phase segregation was suppressed and the I-vacancy concentration in the perovskite decreases[106]. Notably, material stability can decrease significantly when the elastic strain energy in materials is big enough to induce the formation of misfit or dislocation[107, 108].

2. Influence of strain on optoelectronic properties of perovskites

a) Band structure and carrier mobility: Alteration in band structure and carrier mobility with strain have been observed in perovskite materials. In most MHPs, the Pb-I orbital coupling contributes directly to the nature of valence and

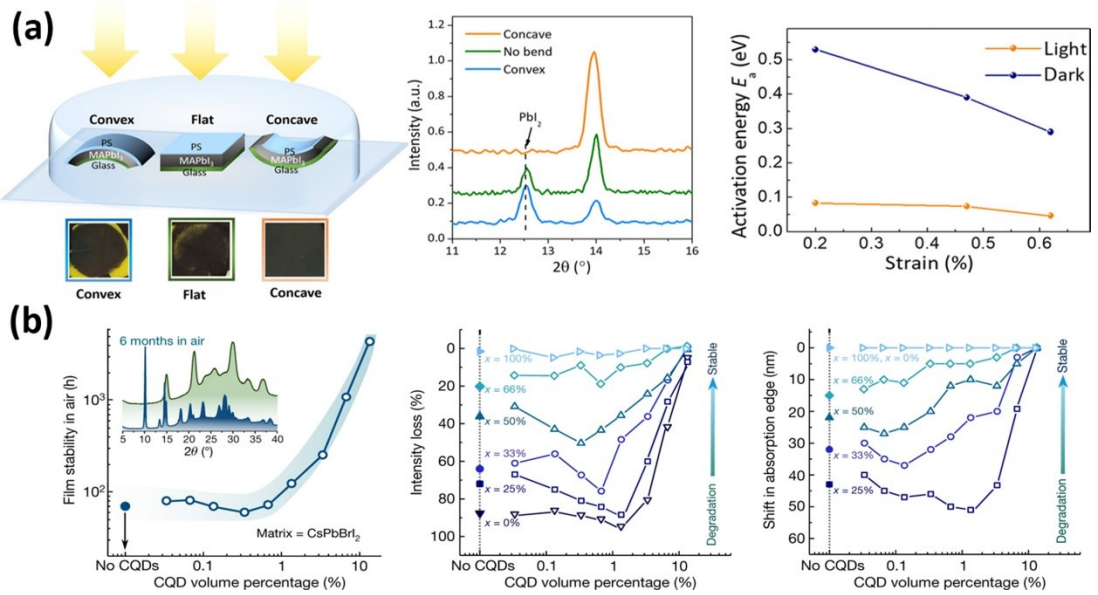

Figure 5. (a), Schematic illustration of the experimental setup applying different strains and resulting photographs of the corresponding $MAPbI_3$ films after 500h of illumination (left); Out-of-plane XRD patterns of the $MAPbI_3$ films with different strains by bending (center) and activation energy of ion migration as a function of the strain level in the $MAPbI_3$ films[34]. Reproduced with permission from Sci Adv 3 (5616) (2017). Copyright 2017 American Association for the Advancement of Science. (b), The intensity loss in absorbance (left) and the shift in the absorption edge (right) after 5 h of annealing in air. x is the Br content. Lattice mismatch increases as decreasing Br content and thus a larger strain is generated at interfaces, a lower PbS CQD concentration results in more perovskite layers between neighboring PbS CQDs and consequently increases the effects of strain[77]. Reproduced with permission from Nature 570, 96-101 (2019). Copyright 2019 Nature Publishing Group.

conduction band edges. The A cations do not contribute directly to the formation of band edges, but their size will influence the Pb-I orbital coupling, thus influencing the valence and conduction band edges indirectly. The valence band maximum (VBM) of perovskite is mainly derived from the strong antibonding coupling between s orbital of Pb and p orbital of I, and the conduction band minimum (CBM) is mainly derived from the coupling of the Pb p orbital with negligible I[3, 109]. Under a tensile strain, the elongation of Pb-I bonds and/or the reduction of Pb-I-Pb angles will decrease the antibonding overlap between the Pb 6s and I 5p orbitals, causing the downshift of VBM and thus the broadening of the bandgap. Under a compressive strain, the shortened Pb-I bonds will enhance the coupling between the Pb s and I p orbitals and lift the VBM, resulting in a reduction of the bandgap. With the further increase of the compressive strain, the decrease of Pb-I-Pb bond angles and resulting inorganic octahedral tilting start to dominate, which will weaken the Pb 6s and I 5p orbital overlap, thereby downshifting the VBM and increasing the perovskite bandgap[106, 110, 111]. Cases where strain alters the bandgap have been reported. When the hydrostatic pressure of 2.1 GPa was applied to the α-$FAPbI_3$ single crystal, its band gap reduced from 1.489 eV to 1.337 eV[112]. Tu et al. applied in-plane uniaxial tensile strain to $(CH_3(CH_2)_3NH_3)_2(CH_3{-}NH_3)_{n-1}Pb_nI_{3n+1}$ 2D perovskite flakes and founded that its band gap increases as the strain increases, and the strain response of bandgap could be as high as 13.3 meV for one percent of strain[85]. The photoluminescence peak of sub-100-nm epitaxial α-$FAPbI_3$ thin films gradually shifted from about 1.523 eV at 0% strain to about 1.488 eV at −2.4% strain, corresponding to a reduction of about 35 meV in the bandgap[73]. Clearly, the changes in bandgap under strain are different and dependent on the composition of the perovskite.

Change of the carrier mobility as a function of strain has also been studied[73, 113, 114]. **Figure 6a** shows the calculated effective mass (m^*) of electron and hole of a α-$FAPbI_3$ perovskite and the band structures of the perovskite with the strains of 3%, 0% and −3%[73]. The effective mass of electron (m_e^*) remains basically unchanged with the change in strain, while the effective mass of hole (m_h^*) decreases considerably with the increase of the compressive strain. The reduced m_h^* under compressive strain enhances the hole mobility until the compressive strain up to -1.2%, as measured from Hall effect measurements and time-of-flight measurements in **Figure 6b-c**[73]. The sharp drop in hole mobility above -1.2 % strain is attributed to the higher dislocation density at higher strains.

In MHPs, the spin-orbit coupling effect contributes strongly to the band splitting in perovskites at different strain due to the existence of the heavy Pb or Sn atoms[115, 116]. Strain induces transition between direct and indirect bandgap in perovskite due to the different spin-splitting behaviors of CBM and VBM[117, 118]. Ghosh et al. used ab initio simulations to investigate the Rashba-splitting effect and the structural property of $FA_{0.75}Cs_{0.25}PbI_3$ under hydrostatic pressure and proposed that there was a direct-indirect bandgap transition in $FA_{0.75}Cs_{0.25}PbI_3$ under 3 GPa, and the resulting indirect bandgap was 5-7 meV narrower than the direct gap[115]. Differently, an indirect-direct band gap transition was observed in $MAPbI_3$ single crystal at 325 MPa hydrostatic pressure and the position of the indirect transition was 60 meV below the direct transition. they thought the reduction of Rashba splitting derives from the reduction in local electric field around the Pb atom under pressure[119].

b) Defects: In strained perovskites, the enhancement of Pb-I interaction under compressive strain increases the

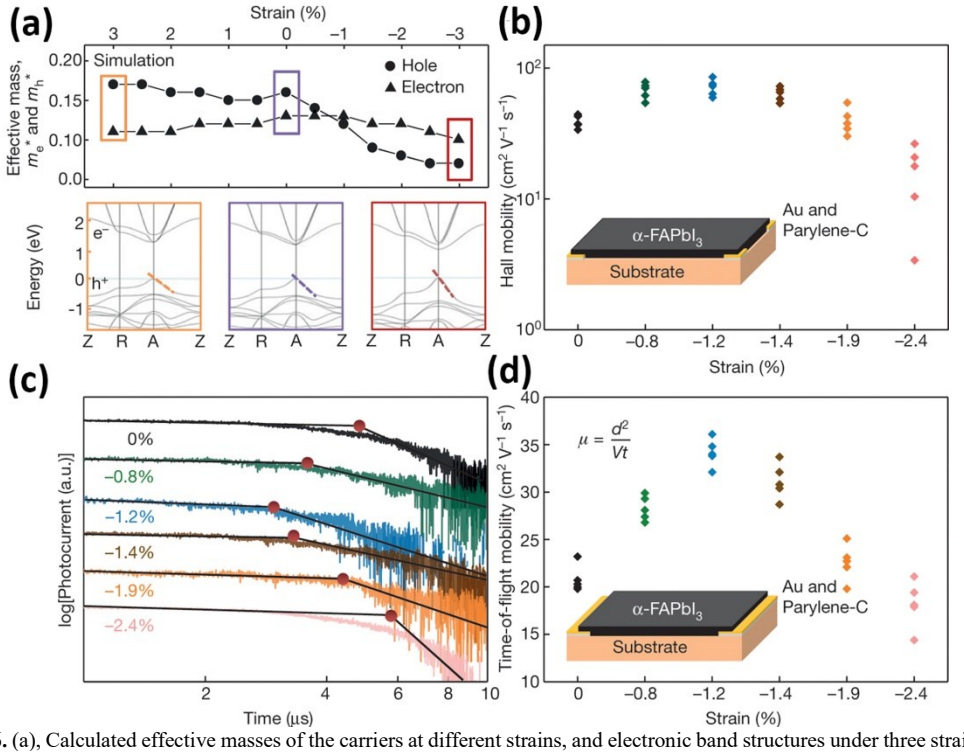

Figure 6. (a), Calculated effective masses of the carriers at different strains, and electronic band structures under three strain levels (3%, 0% and −3%); (b), Hole mobilities by Hall effect measurements under different strain; (c), Transient photocurrent curves of the epitaxial α-FAPbI3 under different strains; (d), Plots of calculated carrier mobilities as a function of the strain magnitudes.[73] Reproduced with permission from Nature 577, 209-215 (2020). Copyright 2020 Nature Publishing Group.

difficulty for I ions to escape from the potential well of Pb atoms, increasing the I migration barrier, which reduces the density of I vacancies and undercoordinated Pb. Conversely, the weaken of Pb-I interaction deriving from the lengthen of Pb-I bonds and shrink of I-Pb-I bond angles may increase the density of I vacancies in perovskites. In perovskite band structures, strain pushes up/down VBM, which will change the trap states. Compressive strain causes the ascendance of the VBM, leading the trap states already existing in the sub-gap close to VBM to become shallower-level defects[106]. Therefore, non-radiative recombination of carriers reduces, and carrier lifetime are improved. Conversely, the trap states shift to a deeper energy level as the VBM shifts downward, increasing non-radiative recombination.

Photoluminescence (PL) spectroscopy is one most convenient technique to characterize the influence of strain to the charge recombination properties of perovskites and thus how strain change defects in perovskites. In strained perovskites, the PL intensity and carrier lifetime were shown to change significantly[65, 106, 120]. Kong et al. reported that the compressed $MAPbI_3$ single crystals exhibited a notable red-shift of its absorption edge under ~0.3 GPa hydrostatic pressure and the band-gap narrowing triggered a 70% to ~100% increase in carrier recombination lifetime[106]. Jones et al. combined synchrotron scanning XRD measurements and local time-resolved PL measurements to study $MAPbI_3$ films and revealed that local strain (tensile strain along in-plane direction) led to an increase of defects such as halide vacancies that are associated with local non-radiative decay. They quantified the trap density with a kinetic model and found that the local strain increased the trap density from $1\times10^{16}cm^{-3}$ to $7.5\times10^{16}cm^{-3}$.[65] Notably, their results did not exclude the influence of grain boundaries, where defect concentration is higher than that of grain interior. Furthermore, in perovskite nanoparticles, Zhao et al. observed that much bigger strain result in more strain-induced defects, leading to lower PL intensity and PL quantum yields (PLQYs) of nano-scale colloidal $CsPbBr_3$ perovskite materials[87].

In addition, in polycrystalline perovskite films, strain was reported to be responsible for the formation of deep trap states and higher non-radiative recombination rate at grain boundaries. Several early calculations based on density functional theory reported that grain boundaries do not introduce deep gap states and are electrically benign[121, 122], which is however against the experimental observations in the field. PL intensity was generally lower at grain boundaries and grain boundaries exhibited a faster nonradiative decay[123]. Hundreds of passivation molecules have been developed to reduce the deep trap densities[124]. After passivation, grain boundaries showed high luminescence efficiencies[125]. Yan et al. considered the impact of the change of bond length or lattice constant at the grain boundary areas on the trap states. Their calculation found that the compressive strain with an increased I–I coupling strength at grain boundaries pushed the I–I antibonding states into the forbidden gap, making iodide interstitial to be deep defect states[126]. Park et al. calculated the energy levels of iodine interstitial defects at $CsPbBr_3$ grain boundaries. They found that when the I-I bond was lengthened at the grain boundaries, the I_i^+/I_i^- levels lowered in energy, making I_i^+ level deeper states with respect to the conduction band edge and I_i^- defects less detrimental than those in the grain interior[127].

IV. Summary and outlook

In summary, strain engineering is a powerful and promising method to control the properties of perovskites. Under strain, the changes in lead-halide bond lengths and halide-lead-halide bond angles will lead to the lattice shrinkage/expansion, or inorganic octahedra framework tilting and lattice rotation in the perovskite. Therefore, strain engineering can be applied to modulate the band structure and carrier dynamics undoubtedly. Meantime, the strain in perovskites will decreasing the energy difference and increases the energy barrier between the perovskite phase and non-perovskite phases, thereby stabilizing the perovskite phase. Strain changes the perovskite material stability due to changes in activation energy of ion migration and trap state energy level. Especially, compressive strain in perovskites increases the activation energy of ion migration, which will hinder the ion migration, thereby inhibiting phase segregation in mixed-halide perovskites.

There are still many open questions to be answered by the perovskite community concerning strain. The first question is about strain relaxation dynamics. Strain in perovskites would eventually be released with the generation of defects such as dislocations or grain boundaries. The second question to be answered is about the strain distribution on microscale. Strain may be inhomogeneous across the halide perovskite films, and the inhomogeneous distribution of strain on in individual grains or across the films may lead to heterogeneity in carrier transport and recombination. Thirdly, there is not enough study yet how the strain is introduced in the perovskite materials. Clearly the solvent evaporation process and thermal treatment would impact the strain formation, and even solar panel encapsulation process may also introduce additional global strain due to the pressure and high temperature to be applied. Finally, strain would also be induced in devices in operation due to the changes of the environmental conditions. Therefore, the development of applicable methods to understand the strain related phenomenon is important for the development of efficient and stable perovskite solar modules with high reliability.

Experiment and Methods:

The simulation of strain distribution: The simulation was conducted by MATLAB. As a first step, we input the geometry of PV modules including different layers using geometric primitives and then the geometry is discretized into a collection of finite element mesh using tetrahedral elements in 3D. Here, each layer is simulated as isotropic material and the mechanical properties of them are shown in Table 2. Boundary conditions are defined according to the PV installation way. In our case, the PV panel was framed at four edges and the mechanical pressure load test with 1000 Pa. At the end, displacement of PV modules was calculated by the partial differential equations (PDE). The PDE toolbox provides functions for solving structural mechanics, heat transfer mechanical deformations, fluid flow and more.

Table 2: Materials of the PV laminate used in the FEM model with the applied material model and thickness.

layer	Materials	Thickness (mm)	Young's modulus (GPa)	Passion's ration (ν)
backsheet	PVF-PET-PVF	0.35	3.5	0.29
encapsulant	EVA	0.45	0.11	0.49
Solar cell	monocrystalline Si	0.2	130	0.28
Front cover	glass	3.2	73	0.23

Acknowledgement: We thank the financial support from the National Science Foundation under awards DMR-1903981 and ECCS-2050357, and the Department of the Defense, Defense Threat Reduction Agency under award HDTRA1-20-2-0002.

Data availability: The data that support the findings of this study are available from the corresponding author upon reasonable request.

Reference:

1. G. E. E. Samuel D. Stranks, 1 Giulia Grancini,2 Christopher Menelaou,1 and T. L. Marcelo J. P. Alcocer, 1 Laura M. Herz,1 Annamaria Petrozza,2 Henry J. Snaith1*, Science **342**, 341-344 (2013).
2. G. E. Eperon, S. D. Stranks, C. Menelaou, M. B. Johnston, L. M. Herz and H. J. Snaith, Energy & Environmental Science **7** (3) (2014).
3. W.-J. Yin, T. Shi and Y. Yan, Applied Physics Letters **104** (6), 063903 (2014).
4. D. Shi, V. Adinolfi, R. Comin, M. Yuan, E. Alarousu, A. Buin, Y. Chen, S. Hoogland, A. Rothenberger, K. Katsiev, Y. Losovyj, X. Zhang, P. A. Dowben, O. F. Mohammed, E. H. Sargent and O. M. Bakr, Science **347** (6221), 519-522 (2015).
5. M. M. Lee, J. Teuscher, T. Miyasaka, T. N. Murakami and H. J. Snaith, Science **338** (6107), 643-647 (2012).
6. L. Protesescu, S. Yakunin, M. I. Bodnarchuk, F. Krieg, R. Caputo, C. H. Hendon, R. X. Yang, A. Walsh and M. V. Kovalenko, Nano Letters **15** (6), 3692-3696 (2015).
7. M. J. Carnie, C. Charbonneau, M. L. Davies, J. Troughton, T. M. Watson, K. Wojciechowski, H. Snaith and D. A. Worsley, Chem Commun (Camb) **49** (72), 7893-7895 (2013).
8. J. Burschka, N. Pellet, S. J. Moon, R. Humphry-Baker, P. Gao, M. K. Nazeeruddin and M. Gratzel, Nature **499** (7458), 316-319 (2013).
9. D. Liu and T. L. Kelly, Nature Photonics **8** (2), 133-138 (2013).
10. L. Dou, Y. M. Yang, J. You, Z. Hong, W. H. Chang, G. Li and Y. Yang, Nat Commun **5**, 5404 (2014).
11. V. Adinolfi, O. Ouellette, M. I. Saidaminov, G. Walters, A. L. Abdelhady, O. M. Bakr and E. H. Sargent, Adv Mater **28** (33), 7264-7268 (2016).
12. W. Q. Wu, Z. Yang, P. N. Rudd, Y. Shao, X. Dai, H. Wei, J. Zhao, Y. Fang, Q. Wang, Y. Liu, Y. Deng, X. Xiao, Y. Feng and J. Huang, Sci Adv **5** (3), eaav8925 (2019).
13. A. Kojima, K. Teshima, Y. Shirai and T. Miyasaka, J Am Chem Soc **131** (17), 6050-6051 (2009).
14. NREL, *Best Research-Cell Efficiency Chart*. (2021). https://www.nrel.gov/pv/cell-efficiency.html
15. C. S. Smith, Physical Review **94** (1), 42-49 (1954).
16. J. Welser, J. L. Hoyt, S. Takagi and J. F. Gibbons, Proceedings of 1994 IEEE International Electron Devices Meeting, 1994, pp. 373-376
17. J. Feng, X. Qian, C.-W. Huang and J. Li, Nature Photonics **6** (12), 866-872 (2012).
18. G. Tsutsui, S. Mochizuki, N. Loubet, S. W. Bedell and D. K. Sadana, AIP Advances **9** (3) (2019).
19. L. Mao, Q. Meng, A. Ahmad and Z. Wei, Advanced Energy Materials **7** (23), 1700535 (2017).
20. D. Djomani, F. Capitani, J. B. Brubach, E. Calandrini, C. Renard, D. Bouchier, J. P. Itie, P. Roy and L. Vincent, Nanotechnology **31** (23), 235711 (2020).
21. L. Vincent, D. Djomani, M. Fakfakh, C. Renard, B. Belier, D. Bouchier and G. Patriarche, Nanotechnology **29** (12), 125601 (2018).
22. J. Berry, S. Zhou, J. Han, D. J. Srolovitz and M. P. Haataja, Nano Lett **17** (4), 2473-2481 (2017).
23. S. Song, D. H. Keum, S. Cho, D. Perello, Y. Kim and Y. H. Lee, Nano Lett **16** (1), 188-193 (2016).
24. Y. M. Niquet, C. Delerue and C. Krzeminski, Nano Lett **12** (7), 3545-3550 (2012).
25. M. Hosseini, M. Elahi, M. Pourfath and D. Esseni, IEEE Transactions on Electron Devices **62** (10), 3192-3198 (2015).
26. H. J. Conley, B. Wang, J. I. Ziegler, R. F. Haglund, Jr., S. T. Pantelides and K. I. Bolotin, Nano Lett **13** (8), 3626-3630 (2013).
27. H. Li, C. Tsai, A. L. Koh, L. Cai, A. W. Contryman, A. H. Fragapane, J. Zhao, H. S. Han, H. C. Manoharan, F. Abild-Pedersen, J. K. Norskov and X. Zheng, Nat Mater **15** (3), 364 (2016).
28. J. R. Petrie, H. Jeen, S. C. Barron, T. L. Meyer and H. N. Lee, J Am Chem Soc **138** (23), 7252-7255 (2016).
29. R. U. Chandrasena, W. Yang, Q. Lei, M. U. Delgado-Jaime, K. D. Wijesekara, M. Golalikhani, B. A. Davidson, E. Arenholz, K. Kobayashi, M. Kobata, F. M. de Groot, U. Aschauer, N. A. Spaldin, X. Xi and A. X. Gray, Nano Lett **17** (2), 794-799 (2017).
30. Y. Rakita, S. R. Cohen, N. K. Kedem, G. Hodes and D. Cahen, MRS Communications **5** (4), 623-629 (2015).

31. A. Ferreira, A. Létoublon, S. Paofai, S. Raymond, C. Ecolivet, B. Rufflé, S. Cordier, C. Katan, M. I. Saidaminov and A. Zhumekenov, Physical review letters **121** (8), 085502 (2018).
32. S. Sun, Y. Fang, G. Kieslich, T. J. White and A. K. Cheetham, Journal of Materials Chemistry A **3** (36), 18450-18455 (2015).
33. J. Feng, APL Materials 2, 081801 (2014).
34. J. Zhao, Y. Deng, H. Wei, X. Zheng, Z. Yu, Y. Shao, J. E. Shield and J. Huang, Sci Adv **3** (5616) (2017).
35. N. Rolston, K. A. Bush, A. D. Printz, A. Gold-Parker, Y. C. Ding, M. F. Toney, M. D. McGehee and R. H. Dauskardt, Advanced Energy Materials **8** (29) (2018).
36. M. I. Saidaminov, J. Kim, A. Jain, R. Quintero-Bermudez, H. Tan, G. Long, F. Tan, A. Johnston, Y. Zhao, O. Voznyy and E. H. Sargent, Nature Energy **3** (8), 648-654 (2018).
37. O. Nakatsuka, H. Kitada, Y. Kim, Y. Mizushima, T. Nakamura, T. Ohba and S. Zaima, Japanese Journal of Applied Physics **50** (5S1), 05ED03 (2011).
38. M. Song, K. R. Mundboth, J. A. Szpunar, L. Chen and R. Feng, Journal of Micromechanics and Microengineering **25** (8), 085002 (2015).
39. M. J. Hÿtch and A. M. Minor, MRS Bulletin **39** (2), 138-146 (2014).
40. S. Chen and P. Gao, Journal of Applied Physics **128** (1), 010901 (2020).
41. Y. Li, W. Zhou, Y. Li, W. Huang, Z. Zhang, G. Chen, H. Wang, G.-H. Wu, N. Rolston and R. Vila, Joule **3** (11), 2854-2866 (2019).
42. M. U. Rothmann, J. S. Kim, J. Borchert, K. B. Lohmann, C. M. O'Leary, A. A. Sheader, L. Clark, H. J. Snaith, M. B. Johnston, P. D. Nellist and L. M. Herz, Science **370** (6516), eabb5940 (2020).
43. V. Ozdol, C. Gammer, X. Jin, P. Ercius, C. Ophus, J. Ciston and A. Minor, Applied Physics Letters **106** (25), 253107 (2015).
44. J. R. Ferraro, K. Nakamoto, Academic Press: New York, 1994
45. C. Rice, R. J. Young, R. Zan, U. Bangert, D. Wolverson, T. Georgiou, R. Jalil and K. S. Novoselov, Physical Review B **87** (8) (2013).
46. M. A. Bissett, M. Tsuji and H. Ago, Phys Chem Chem Phys **16** (23), 11124-11138 (2014).
47. C. Fasolato, M. De Luca, D. Djomani, L. Vincent, C. Renard, G. Di Iorio, V. Paillard, M. Amato, R. Rurali and I. Zardo, Nano Lett **18** (11), 7075-7084 (2018).
48. B. Fluegel, A. V. Mialitsin, D. A. Beaton, J. L. Reno and A. Mascarenhas, Nat Commun **6**, 7136 (2015).
49. K. Talit and D. A. Strubbe, The Journal of Physical Chemistry C 124 (50), 27287-27299 (2020).
50. A. Ogura, D. Kosemura, M. Takei, H. Uchida, N. Hattori, M. Yoshimaru, S. Mayuzumi and H. Wakabayashi, Materials Science and Engineering: B **159**, 206-211 (2009).
51. M. Ledinský, P. Löper, B. Niesen, J. Holovský, S.-J. Moon, J.-H. Yum, S. De Wolf, A. Fejfar and C. Ballif, The Journal of Physical Chemistry Letters **6** (3), 401-406 (2015).
52. M. Ledinský, E. Moulin, G. Bugnon, K. Ganzerová, A. Vetushka, F. Meillaud, A. Fejfar and C. Ballif, Applied Physics Letters **105** (11), 111106 (2014).
53. K. Kitahara, A. Moritani, A. Hara and M. Okabe, Japanese journal of applied physics **38** (11B), L1312 (1999).
54. C. Li, X. Lu, W. Ding, L. Feng, Y. Gao and Z. Guo, Acta Crystallographica Section B: Structural Science **64** (6), 702-707 (2008).
55. W. Travis, E. N. K. Glover, H. Bronstein, D. O. Scanlon and R. G. Palgrave, Chem Sci 7 (7), 4548-4556 (2016).
56. X. Zheng, C. Wu, S. K. Jha, Z. Li, K. Zhu and S. Priya, ACS Energy Letters **1** (5), 1014-1020 (2016).
57. C. Wu, K. Chen, D. Guo, S. Wang and P. Li, RSC advances **8** (6), 2900-2905 (2018).
58. H. Wang, C. Zhu, L. Liu, S. Ma, P. Liu, J. Wu, C. Shi, Q. Du, Y. Hao, S. Xiang, H. Chen, P. Chen, Y. Bai, H. Zhou, Y. Li and Q. Chen, Adv Mater **31** (48), e1904408 (2019).
59. G. Kim, H. Min, K. S. Lee, D. Y. Lee, S. M. Yoon and S. I. Seok, Science **370** (6512), 4 (2020).
60. E. T. Hoke, D. J. Slotcavage, E. R. Dohner, A. R. Bowring, H. I. Karunadasa and M. D. McGehee, Chemical Science **6** (1), 613-617 (2015).
61. J.-S. Park and A. Walsh, Annual Review of Condensed Matter Physics **12**, 95-109 (2020).
62. H. Tsai, R. Asadpour, J.-C. Blancon, C. C. Stoumpos, O. Durand, J. W. Strzalka, B. Chen, R. Verduzco, P. M. Ajayan and S. Tretiak, Science **360** (6384), 67-70 (2018).
63. B. Chen, J. Song, X. Dai, Y. Liu, P. N. Rudd, X. Hong and J. Huang, Adv Mater **31** (35), e1902413 (2019).
64. K. A. Bush, N. Rolston, A. Gold-Parker, S. Manzoor, J. Hausele, Z. J. Yu, J. A. Raiford, R. Cheacharoen, Z. C. Holman, M. F. Toney, R. H. Dauskardt and M. D. McGehee, ACS Energy Letters **3** (6), 1225-1232 (2018).
65. T. W. Jones, A. Osherov, M. Alsari, M. Sponseller, B. C. Duck, Y.-K. Jung, C. Settens, F. Niroui, R. Brenes and C. V. Stan, Energy & Environmental Science **12** (2), 596-606 (2019).
66. X. Li, Y. Luo, M. V. Holt, Z. Cai and D. P. Fenning, Chemistry of Materials **31** (8), 2778-2785 (2019).
67. D. H. Fabini, C. C. Stoumpos, G. Laurita, A. Kaltzoglou, A. G. Kontos, P. Falaras, M. G. Kanatzidis and R. Seshadri, Angewandte Chemie International Edition **55** (49), 15392-15396 (2016).
68. L. Cojocaru, S. Uchida, Y. Sanehira, V. Gonzalez-Pedro, J. Bisquert, J. Nakazaki, T. Kubo and H. Segawa, Chemistry Letters **44** (11), 1557-1559 (2015).

69. T. J. Jacobsson, L. J. Schwan, M. Ottosson, A. Hagfeldt and T. Edvinsson, Inorganic Chemistry **54** (22), 10678-10685 (2015).
70. C. Ge, M. Hu, P. Wu, Q. Tan, Z. Chen, Y. Wang, J. Shi and J. Feng, The Journal of Physical Chemistry C **122** (28), 15973-15978 (2018).
71. J. A. Steele, H. Jin, I. Dovgaliuk, R. F. Berger, T. Braeckevelt, H. Yuan, C. Martin, E. Solano, K. Lejaeghere and S. M. Rogge, Science **365** (6454), 679-684 (2019).
72. D. J. Xue, Y. Hou, S. C. Liu, M. Wei, B. Chen, Z. Huang, Z. Li, B. Sun, A. H. Proppe, Y. Dong, M. I. Saidaminov, S. O. Kelley, J. S. Hu and E. H. Sargent, Nat Commun **11** (1), 1514 (2020).
73. Y. Chen, Y. Lei, Y. Li, Y. Yu, J. Cai, M.-H. Chiu, R. Rao, Y. Gu, C. Wang and W. Choi, Nature **577** (7789), 209-215 (2020).
74. E. Oksenberg, A. Merdasa, L. Houben, I. Kaplan-Ashiri, A. Rothman, I. G. Scheblykin, E. L. Unger and E. Joselevich, Nat Commun **11** (1), 489 (2020).
75. E. Shi, B. Yuan, S. B. Shiring, Y. Gao, Akriti, Y. Guo, C. Su, M. Lai, P. Yang, J. Kong, B. M. Savoie, Y. Yu and L. Dou, Nature **580** (7805), 614-620 (2020).
76. J.-W. Lee, S. Tan, T.-H. Han, R. Wang, L. Zhang, C. Park, M. Yoon, C. Choi, M. Xu, M. E. Liao, S.-J. Lee, S. Nuryyeva, C. Zhu, K. Huynh, M. S. Goorsky, Y. Huang, X. Pan and Y. Yang, Nat Commun 11 (1), 5514 (2020).
77. M. Liu, Y. Chen, C.-S. Tan, R. Quintero-Bermudez, A. H. Proppe, R. Munir, H. Tan, O. Voznyy, B. Scheffel, G. Walters, A. P. T. Kam, B. Sun, M.-J. Choi, S. Hoogland, A. Amassian, S. O. Kelley, F. P. García De Arquer and E. H. Sargent, Nature **570** (7759), 96-101 (2019).
78. Y. Zhao, J. Duan, Y. Wang, X. Yang and Q. Tang, Nano Energy **67**, 104286 (2020).
79. Y. Fu, M. P. Hautzinger, Z. Luo, F. Wang, D. Pan, M. M. Aristov, I. A. Guzei, A. Pan, X. Zhu and S. Jin, ACS Central Science **5** (8), 1377-1386 (2019).
80. S. Ma, S. H. Kim, B. Jeong, H. C. Kwon, S. C. Yun, G. Jang, H. Yang, C. Park, D. Lee and J. Moon, Small **15** (21), e1900219 (2019).
81. L. A. Muscarella, E. M. Hutter, F. Wittmann, Y. W. Woo, Y. Jung, L. McGovern, J. Versluis, A. Walsh, H. J. Bakker and B. Ehrler, ACS Energy Lett 5 (10), 3152-3158 (2020).
82. L. Zhang, L. Wang, K. Wang and B. Zou, The Journal of Physical Chemistry C **122** (27), 15220-15225 (2018).
83. W. Kim, M. S. Jung, S. Lee, Y. J. Choi, J. K. Kim, S. U. Chai, W. Kim, D.-G. Choi, H. Ahn, J. H. Cho, D. Choi, H. Shin, D. Kim and J. H. Park, Advanced Energy Materials **8** (10) (2018).
84. G. Liu, L. Kong, W. Yang and H.-k. Mao, Materials Today **27**, 91-106 (2019).
85. Q. Tu, I. Spanopoulos, S. Hao, C. Wolverton, M. G. Kanatzidis, G. S. Shekhawat and V. P. Dravid, ACS Energy Letters **4** (3), 796-802 (2019).
86. Q. Zhao, A. Hazarika, L. T. Schelhas, J. Liu, E. A. Gaulding, G. Li, M. Zhang, M. F. Toney, P. C. Sercel and J. M. Luther, ACS Energy Letters **5** (1), 238-247 (2020).
87. J. Zhao, M. Liu, L. Fang, S. Jiang, J. Zhou, H. Ding, H. Huang, W. Wen, Z. Luo, Q. Zhang, X. Wang and C. Gao, J Phys Chem Lett **8** (13), 3115-3121 (2017).
88. V. Wadhawan, Bulletin of Materials Science **6** (4), 733-753 (1984).
89. E. K. Salje, Annual Review of Materials Research **42**, 265-283 (2012).
90. T.-C. Wei, H.-P. Wang, T.-Y. Li, C.-H. Lin, Y.-H. Hsieh, Y.-H. Chu and J.-H. He, Advanced Materials **29** (35), 1701789 (2017).
91. Y. Zhou, L. You, S. Wang, Z. Ku, H. Fan, D. Schmidt, A. Rusydi, L. Chang, L. Wang, P. Ren, L. Chen, G. Yuan, L. Chen and J. Wang, Nature Communications 7 (1), 11193 (2016).
92. N. Rolston, R. Bennett-Kennett, L. T. Schelhas, J. M. Luther, J. A. Christians, J. J. Berry and R. H. Dauskardt, Science 368 (6488), eaay8691 (2020).
93. S. A. Kalogirou, *Solar energy engineering: processes and systems*. (Academic Press, 2013)
94. NASA earth observatory, https://earthobservatory.nasa.gov/biome/biodesert.php.
95. UC museum of paleontology, https://ucmp.berkeley.edu/exhibits/biomes/deserts.php.
96. T. Markvart and A. McEvoy, *Practical handbook of photovoltaics: fundamentals and applications*. (Elsevier, 2003).
97. A. Alateeq, *Buckling Effect on the Performance of Solar Cells under Different Loading Conditions*.(2018). https://lib.dr.iastate.edu/creativecomponents/23/.
98. U. Eitner, *Thermomechanics of photovoltaic modules.* (2011). https://opendata.uni-halle.de/handle/1981185920/7357.
99. M. T. Zarmai, N. N. Ekere, C. F. Oduoza and E. H. Amalu, Robotics and Computer-Integrated Manufacturing **47**, 37-43 (2017).
100. S. Liu, S. Sun, C. K. Gan, A. G. d. Águila, Y. Fang, J. Xing, T. T. H. Do, T. J. White, H. Li, W. Huang and Q. Xiong, Science Advances **5** (9445) (2019).
101. B. Murali, E. Yengel, W. Peng, Z. Chen, M. S. Alias, E. Alarousu, B. S. Ooi, V. Burlakov, A. Goriely and M. Eddaoudi, The journal of physical chemistry letters **8** (1), 137-143 (2017).
102. X. Lu, W. Yang, Q. Jia and H. Xu, Chem Sci **8** (10), 6764-6776 (2017).
103. L. Wang, K. Wang and B. Zou, J Phys Chem Lett **7** (13), 2556-2562 (2016).
104. T. Chen, B. J. Foley, C. Park, C. M. Brown, L. W. Harriger, J. Lee, J. Ruff, M. Yoon, J. J. Choi and S.-H. Lee, Science Advances **2** (10), e1601650 (2016).
105. L. Guo, G. Xu, G. Tang, D. Fang and J. Hong,

arXiv preprint arXiv:2001.01041 (2020).
106. L. Kong, G. Liu, J. Gong, Q. Hu, R. D. Schaller, P. Dera, D. Zhang, Z. Liu, W. Yang and K. Zhu, Proceedings of the National Academy of Sciences **113** (32), 8910-8915 (2016).
107. D. J. DUNSTAN, JOURNAL OF MATERIALS SCIENCE: MATERIALS IN ELECTRONICS **8**, 337—375 (1997).
108. S. R. Lee, D. D. Koleske, K. C. Cross, J. A. Floro, K. E. Waldrip, A. T. Wise and S. Mahajan, Applied Physics Letters **85** (25), 6164-6166 (2004).
109. L.-y. Huang and W. R. Lambrecht, Physical Review B **88** (16), 165203 (2013).
110. R. Prasanna, A. Gold-Parker, T. Leijtens, B. Conings, A. Babayigit, H.-G. Boyen, M. F. Toney and M. D. McGehee, Journal of the American Chemical Society **139** (32), 11117-11124 (2017).
111. C. Grote and R. F. Berger, The Journal of Physical Chemistry C **119** (40), 22832-22837 (2015).
112. G. Liu, L. Kong, J. Gong, W. Yang, H. k. Mao, Q. Hu, Z. Liu, R. D. Schaller, D. Zhang and T. Xu, Advanced Functional Materials **27** (3), 1604208 (2017).
113. Y. Jiao, F. Ma, H. Wang, J. Bell and A. Du, Particle & Particle Systems Characterization **34** (4), 1600288 (2017).
114. C. Zhu, X. Niu, Y. Fu, N. Li, C. Hu, Y. Chen, X. He, G. Na, P. Liu, H. Zai, Y. Ge, Y. Lu, X. Ke, Y. Bai, S. Yang, P. Chen, Y. Li, M. Sui, L. Zhang, H. Zhou and Q. Chen, Nat Commun **10** (1), 815 (2019).
115. D. Ghosh, A. Aziz, J. A. Dawson, A. B. Walker and M. S. Islam, Chemistry of Materials **31** (11), 4063-4071 (2019).
116. J. Yin, P. Maity, L. Xu, A. M. El-Zohry, H. Li, O. M. Bakr, J.-L. Brédas and O. F. Mohammed, Chemistry of Materials **30** (23), 8538-8545 (2018).
117. E. M. Hutter, M. C. Gelvez-Rueda, A. Osherov, V. Bulovic, F. C. Grozema, S. D. Stranks and T. J. Savenije, Nat Mater **16** (1), 115-120 (2017).
118. F. Zheng, L. Z. Tan, S. Liu and A. M. Rappe, Nano letters **15** (12), 7794-7800 (2015).
119. T. Wang, B. Daiber, J. M. Frost, S. A. Mann, E. C. Garnett, A. Walsh and B. Ehrler, Energy & Environmental Science **10** (2), 509-515 (2017).
120. K. M. Boopathi, B. Martín-García, A. Ray, J. M. Pina, S. Marras, M. I. Saidaminov, F. Bonaccorso, F. Di Stasio, E. H. Sargent, L. Manna and A. L. Abdelhady, ACS Energy Letters **5** (2), 642-649 (2020).
121. W.-J. Yin, T. Shi and Y. Yan, Advanced Materials **26** (27), 4653-4658 (2014).
122. W.-J. Yin, J.-H. Yang, J. Kang, Y. Yan and S.-H. Wei, Journal of Materials Chemistry A **3** (17), 8926-8942 (2015).
123. D. W. De Quilettes, S. M. Vorpahl, S. D. Stranks, H. Nagaoka, G. E. Eperon, M. E. Ziffer, H. J. Snaith and D. S. Ginger, Science **348** (6235), 683-686 (2015).
124. B. Chen, P. N. Rudd, S. Yang, Y. Yuan and J. Huang, Chem Soc Rev **48** (14), 3842-3867 (2019).
125. M. Abdi-Jalebi, Z. Andaji-Garmaroudi, S. Cacovich, C. Stavrakas, B. Philippe, J. M. Richter, M. Alsari, E. P. Booker, E. M. Hutter, A. J. Pearson, S. Lilliu, T. J. Savenije, H. Rensmo, G. Divitini, C. Ducati, R. H. Friend and S. D. Stranks, Nature **555** (7697), 497-501 (2018).
126. Y. Yan, W.-J. Yin, T. Shi, W. Meng and C. Feng, in *Organic-Inorganic Halide Perovskite Photovoltaics* (2016), pp. 79-105.
127. J.-S. Park, J. Calbo, Y.-K. Jung, L. D. Whalley and A. Walsh, ACS Energy Letters **4** (6), 1321-1327 (2019).